Research Article

Journal of Environmental Nanotechnology

Green Synthesis of TiO_2 Nanoparticles Using *Ocimum tenuiflorum* and *Wrightia tinctoria* Leaf Extracts: Characterization, Antibacterial Activity, and Machine Learning-Based Cytocompatibility Prediction

P. Rasagopal[1*], S. Aruna Deepthi[2], M. Ramesh[3], D. Mohankumar[4], Ravindra Ramchandra Ghugare[5] and S. Balachandran[6]

[1]Department of Mechanical Engineering, K.S.R. College of Engineering, Tiruchengode, TN, India
[2]Department of Electronics and Communication Engineering, Vasavi College of Engineering, Hyderabad, TG, India
[3]Department of Mechanical Engineering, M.P. Nachimuthu M. Jaganathan Engineering College, Chennimalai, TN, India
[4]Department of Information Technology, Nandha College of Technology, Perundurai, TN, India
[5]Department of Computer Engineering, Bharati Vidyapeeth College of Engineering, Navi Mumbai, MH, India
[6]Department of Chemical Engineering, Vel Tech High Tech Dr. Rangarajan Dr. Sakunthala Engineering College, Chennai, TN, India
Received: 31.07.2026 Accepted: 29.08.2026 Published: 30.09.2026
*ksrcemechprg@gmail.com

ABSTRACT

This study reports the microwave-assisted green synthesis of TiO_2 nanoparticles (TiO_2 NPs) using *Ocimum tenuiflorum* (Tulsi), *Wrightia tinctoria*, and their combined leaf extracts, with titanium (IV) isopropoxide (TTIP) as the titanium precursor. XRD confirmed the formation of anatase TiO_2 without detectable secondary phases, with average crystallite sizes of 13, 15, and 18 nm for the *O. tenuiflorum*, *W. tinctoria*, and combined-extract samples, respectively. The combined-extract sample contained quasi-spherical primary nanoparticles with a comparatively narrow size range of 18–38 nm; however, larger micron-scale agglomerates were observed by FESEM, potentially resulting from particle association during drying. FTIR spectra indicated the involvement of hydroxyl, carbonyl-related, C–O, and C–O–C functional groups in nanoparticle formation and surface stabilization, together with characteristic Ti–O–Ti vibrations. DLS measurements showed hydrodynamic diameters of 103.6, 87.1, and 71.9 nm, with corresponding reported fractions below 100 nm of 57.7%, 85.5%, and 96.5%, respectively. Zeta potentials of −24.8, −27.1, and −31.2 mV suggested progressively stronger electrostatic stabilization under the measurement conditions, although long-term colloidal stability was not evaluated. All TiO_2 NP formulations exhibited concentration-dependent antibacterial activity against *Escherichia coli* DH5α, *Enterobacter* 2282, and *Bacillus subtilis* 1305. At 250 µg mL^{-1}, the combined-extract sample produced the largest inhibition zones of 15, 16, and 14 mm against *E. coli*, *Enterobacter*, and *B. subtilis*, respectively. A gradient boosting regression model was developed using a computationally constructed dataset of 240 observations, representing three TiO_2 NP formulations, ten concentration levels within 10–500 µg mL^{-1}, two exposure periods (24 and 48 h), and four mammalian cell lines—HeLa, HEK-293, J774A.1, and HepG2. Ten-fold cross-validation yielded R^2 = 0.9869, RMSE = 0.8267, MAE = 0.6819, and MAPE = 0.7609%, indicating strong internal predictive performance. These outcomes highlight the effectiveness of plant extracts as sustainable bioresources for TiO_2 NPs with promising biomedical applications.

Keywords: Green synthesis; Plant extract; Zeta potential; Colloidal stability; Biocompatibility.

1. INTRODUCTION

Nanotechnology has emerged as one of the most influential research fields owing to its ability to engineer materials with physicochemical properties that differ significantly from their bulk counterparts. Among nanomaterials, metal oxide nanoparticles have attracted considerable attention because of their high surface area, chemical stability, catalytic activity, and diverse functional applications. TiO_2 nanoparticles have been widely investigated for antimicrobial, photocatalytic, biomedical, biosensing, and drug-delivery applications because of their chemical stability and functional surface properties (Ansari and Daneshjou, 2024). However, their biological compatibility is not universal and may depend on nanoparticle size, concentration, surface characteristics, exposure duration, and biological system; therefore, cytocompatibility should be evaluated for the specific formulation and exposure conditions employed (Banerjee *et al.* 2023).

Green synthesis has emerged as a promising strategy for producing metal oxide nanoparticles using plant-derived phytochemicals that can assist nanoparticle formation and stabilization (Blessymol *et al*. 2023). This approach reduces the need for conventional reducing and stabilizing reagents by employing plant-derived constituents. Plant extracts were rich in alkaloids,

flavonoids, terpenoids, tannins, proteins, phenolic acids, and bioactive metabolites that facilitate nanoparticle formation and enhance their biological activities. Consequently, biogenic synthesis has gained considerable attention as an environmentally benign and economically viable alternative for fabricating functional nanomaterials with enhanced biomedical performance. Within this context, TiO_2 represents a relevant metal oxide for developing antibacterial nanomaterials, while plant-extract-mediated synthesis offers a route for introducing naturally derived surface-associated functional groups. *O. tenuiflorum* and *W. tinctoria* were selected as phytochemical sources, and their individual and combined effects were compared systematically. Because nanoparticle physicochemical characteristics can influence both antibacterial activity and mammalian-cell responses, the present study integrates material characterization, antibacterial testing, and computational cytocompatibility prediction within a focused experimental framework.

Previous studies demonstrate that plant-mediated synthesis can produce functional metal-oxide nanoparticles with antibacterial, antioxidant, photocatalytic, and biomedical properties. In particular, *W. tinctoria* has been used for ZrO_2 and ZnO synthesis, while *O. tenuiflorum* has served as a phytochemical source in ZnO-containing biomedical materials. However, these studies predominantly examine other oxide systems or single-plant routes, leaving limited understanding of how individual and combined *O. tenuiflorum–W. tinctoria* extracts influence TiO_2 nanoparticle characteristics and biological performance. Plant-derived phytochemicals play a vital role in nanoparticle formation and surface stabilization. Ultrasound-assisted extracts of sapote peels exhibited enhanced phytochemical content, with black sapote extract achieving 10.72 mg GAE/g total polyphenols and 4.77 mg QE/g flavonoids, while antibiofilm inhibition against Pseudomonas aeruginosa at 800 µg/mL, and molecular docking confirmed strong interactions of phenolic compounds with the LasR protein (Silva-Jara *et al.* 2026).

Medicinal plant-mediated nanoparticles have demonstrated remarkable therapeutic potential in recent years. Green-synthesized silver nanoparticles using Calotropis gigantea leaf exhibited spherical particles of 11–17 nm with a −30.2 mV zeta potential and produced a 16.00 ± 0.17 mm inhibition zone against Helicobacter pylori (Kamalesan *et al.* 2026). Green-synthesized bismuth nanoparticles by *Endocomia macrocoma* leaf extract exhibited spherical morphology with particle sizes of 30–60 nm, an average hydrodynamic size of 99.1 nm, a 21.34 mV zeta potential, antibacterial activity with a 250 µg/mL MIC, and antioxidant activity with a DPPH IC_{50} of 125 µg/mL (Shivappa *et al.* 2025). Silver nanoparticles synthesized using *Tribulus terrestris* leaf extract exhibited strong antioxidant activities of 78.27% (DPPH), 76.55% (ABTS) (Rachel *et al.* 2025).

Various metal oxide nanomaterials, such as zinc oxide nanoparticles, have received considerable attention because of their excellent antimicrobial and antioxidant properties. Green-synthesized ZnO nanoparticles using *Garcinia cowa* leaf extract exhibited effective antibacterial activity against *Bacillus subtilis* and *Pseudomonas aeruginosa*, and strong molecular docking affinities of −4.9 and −5.1 kcal/mol with favorable ADMET profiles (Chowdhury *et al.* 2026). Green-synthesized ZnO nanoparticles using Oxalis stricta leaf extract exhibited potent anticancer activity against colon cancer cells with an IC_{50} of 30.27 µg/mL, and molecular docking demonstrated strong interactions with MMP-9, GSK3β, and Bcr-Abl, highlighting their promise as multi-targeted nanotherapeutics (Chandramohan *et al.* 2025).

Previous work with *Wrightia tinctoria* has demonstrated its suitability for plant-mediated synthesis of ZrO_2 and ZnO nanoparticles with antibacterial activity (Al-Zaqri *et al.* 2021); (Kavikala *et al.* 2023). Similarly, *Ocimum tenuiflorum* -derived phytochemicals have been successfully employed in green nanoparticle systems for biomedical applications (Kadri *et al.* 2026). These findings provide the basis for evaluating both extracts as phytochemical mediators during TiO_2 synthesis. Titanium dioxide nanoparticles themselves have attracted enormous interest owing to their excellent catalytic efficiency and biological compatibility. TiO_2 nanoparticles enabled an eco-friendly multicomponent synthesis of pyrimidine derivatives that exhibited remarkable anti-inflammatory and antioxidant activities, while molecular docking, pharmacokinetic, SAR, and DFT analyses confirmed favorable biological interactions and therapeutic potential of the synthesized compounds (Shehab *et al.* 2025). Green-synthesized TiO_2–ZnO nanocomposites using *Parkia timoriana* exhibited an average crystallite size of 38 nm, an A549 lung cancer IC_{50} of 37.07 µg/mL, nearly 100% drug release within 24 h, potent antibacterial activity against multidrug-resistant pathogens, and strong molecular docking interactions with bacterial and lung cancer proteins, demonstrating excellent potential for biomedical applications (Silambarasan *et al.* 2026).

Despite increasing research on plant-mediated metal-oxide synthesis, limited information is available on the comparative preparation of TiO_2 nanoparticles using *O. tenuiflorum* extract, *W. tinctoria* extract, and their combined extract under identical synthesis conditions. In particular, their comparative effects on crystallite size, hydrodynamic diameter, zeta potential, morphology, antibacterial performance, and predicted cytocompatibility remain insufficiently investigated. The novelty of this study lies in directly comparing three microwave-assisted TiO_2 synthesis routes: *O. tenuiflorum* extract alone, *W. tinctoria* extract alone, and a 1:1 (v/v) combination of both extracts, while maintaining identical precursor and processing

conditions. The study further integrates physicochemical characterization, antibacterial testing, and gradient-boosting-based cytocompatibility prediction within a single framework. Intermittent microwave treatment limited continuous thermal exposure and was selected to support controlled TTIP hydrolysis, condensation, nucleation, and particle growth. The synthesis incorporates greener elements through the use of aqueous plant extracts as phytochemical-assisted reaction media; however, it is not described as completely green because TTIP, ethanol, microwave energy, washing, and drying remain part of the process. Three TiO_2 NP formulations were investigated: one synthesized using *O. tenuiflorum* extract, one using *W. tinctoria* extract, and one using their 1:1 (v/v) combined extract.

2. MATERIALS AND METHODOLOGY

2.1 Materials

Green synthesis of TiO_2 NPs was carried out using aqueous leaf extracts of Ocimum tenuiflorum (Tulsi) and Wrightia tinctoria as natural phytochemical sources, while Titanium(IV) isopropoxide (TTIP, 97% purity) served as the titanium precursor. Ethanol (C_2H_5OH, 99.5% purity) was used during precursor preparation and washing steps. Fresh leaves of both plant species were collected from the Forest region of Sathyamangalam Reserve Forest, Erode, India. All chemicals was of analytical grade and as received without purification. Deionized water was employed throughout synthesis and purification procedures.

2.2 Methodology

Fresh leaves of *Ocimum tenuiflorum* and *Wrightia tinctoria* were collected and washed with deionized water to eliminate dust and surface impurities, and dried in a hot-air oven at 60 °C. Dried leaves were ground into fine powder using a laboratory grinder (Han *et al.* 2023). To prepare each plant extract, 5 g of dried leaf powder was dispersed in 70 mL of distilled water and heated at 80 °C for 30 min under continuous stirring. The resulting extract, with a nominal leaf-powder concentration of approximately 71.4 mg mL^{-1}, was cooled to room temperature, filtered, and stored at 4 °C until use. The extract was cooled, filtered, and stored for subsequent synthesis. For the mixed-extract system, equal volumes of *Ocimum tenuiflorum* and *Wrightia tinctoria* extracts were blended in a 1:1 (v/v) ratio. Three synthesis formulations were investigated: TiO_2 NPs prepared using *O. tenuiflorum* extract, *W. tinctoria* extract, and a 1:1 (v/v) mixture of both extracts. Each formulation was synthesized in three independent batches (n = 3), giving nine independently prepared nanoparticle batches. Identical precursor volume, extract-to-precursor ratio, pH, stirring, microwave-treatment, washing, and drying conditions were maintained for all formulations. During nanoparticle synthesis, 7 mL of the prepared extract was added dropwise to 70 mL of undiluted TTIP (97%; approximately 3.28 mol L^{-1}, calculated using a density of 0.96 g mL^{-1}) under continuous magnetic stirring. A few drops of ethanol were added to improve precursor dispersion and minimize microbial contamination during extract storage. Phytochemicals in plant extracts facilitated hydrolysis, condensation, and stabilization of the resulting TiO_2 nanoparticles (TiO_2 NPs). The schematic illustration of the overall synthesis procedure is shown in Fig. 1.

Following the dropwise addition of the plant extract to the TTIP precursor, the reaction mixture was continuously stirred for 2 h at ambient temperature to promote controlled hydrolysis and condensation. The reaction mixture was subsequently treated using a Discover 2.0 microwave synthesis reactor operated at 300 W. Microwave irradiation was applied through nine cycles, each comprising 20 s of irradiation followed by a 20 s power-off interval. This provided a cumulative irradiation time of 180 s and a total cycle duration of 360 s. The maximum reaction temperature was maintained at 180 °C and monitored using the integrated infrared temperature sensor. After microwave treatment, the reaction vessel was cooled to room temperature before centrifugation. The resulting suspension was centrifuged at 2500 rpm for 15 minutes, and the precipitate was repeatedly washed with ethanol and deionized water to eliminate unreacted precursor and residual impurities (Ganvir *et al.* 2026). The purified product was dried at 65 °C for 2.5 h, maintaining a reaction pH of approximately 6 throughout the synthesis. The dried powder was further oven-dried at 40 °C for 1 day, gently ground with a pestle and mortar, and finally dispersed in a water bath before characterization. A schematic representation of the proposed formation mechanism of TiO_2 NPs.

2.3 Material Characterization

2.3.1 DLS Analysis

Hydrodynamic particle size distribution of TiO_2 was determined by Zetasizer Nano ZS based on the DLS technique. This method estimates particle size by fluctuations in scattered laser light caused Brownian motion of nanoparticles suspended at liquid medium. Average hydrodynamic diameter and particle size distribution were obtained directly from the recorded scattering intensity.

Colloidal stability and surface charge of TiO_2 NP suspension were evaluated by the same instrument operated in electrophoretic light scattering (ELS) mode. The measured zeta potential represents the electrical potential at the slipping plane surrounding dispersed nanoparticles and serves as an indicator of suspension stability. Absolute zeta potential values correspond to stronger electrostatic repulsion and improved dispersion

stability, whereas values approaching zero indicate an increased tendency for particle agglomeration and sedimentation.

2.3.2 X-ray Diffraction

Crystalline phase and structural properties of TiO_2 NPs were characterized by XRD (Bruker D8 Advance) with Cu Kα radiation (λ = 1.5406 Å). Diffraction patterns were collected over a 2θ range of 20°–90° with a scanning rate of 2° min^{-1}. The average crystallite size was estimated by the Debye–Scherrer equation (Najm *et al.* 2026).

$$D = \frac{K\lambda}{\beta \cos\theta} \quad \ldots (1)$$

In the Debye–Scherrer equation, D is the crystallite size, K is the shape factor (0.90), λ is the Cu Kα wavelength (0.15406 nm), β is the instrument-corrected full width at half maximum in radians, and θ is the Bragg angle. Instrumental broadening was corrected using β=(β2observed−β2instrument)1/2, with a standard crystalline reference used to determine βinstrument. Calculations were performed using the dominant anatase (101) reflection at 2θ = 25.30°.

2.3.3 FTIR Analysis

The surface functional groups of TiO_2 were analyzed using a PerkinElmer Spectrum Two FTIR spectrometer. Spectra were recorded over the range of 4000–500 cm^{-1} with a spectral resolution of 4 cm^{-1} (Ponnuswamy *et al.* 2024). FTIR was performed to identify phytochemical groups involved in nanoparticle formation and stabilization and to verify the presence of Ti–O–Ti bonding.

2.3.4 FESEM and EDS Analysis

SEM of synthesized TiO_2 NPs was examined using a Gemini Zeiss field-emission scanning electron microscope. High-resolution micrographs were obtained to evaluate particle morphology, size distribution, and surface characteristics (Krishnasamy *et al.* 2026). The elemental composition was determined by an integrated EDX spectroscopy detector, while elemental mapping was performed to examine the spatial distribution of titanium and oxygen within nanoparticles. Before analysis, samples were sputter-coated with a thin platinum layer to raise electrical conductivity and image quality.

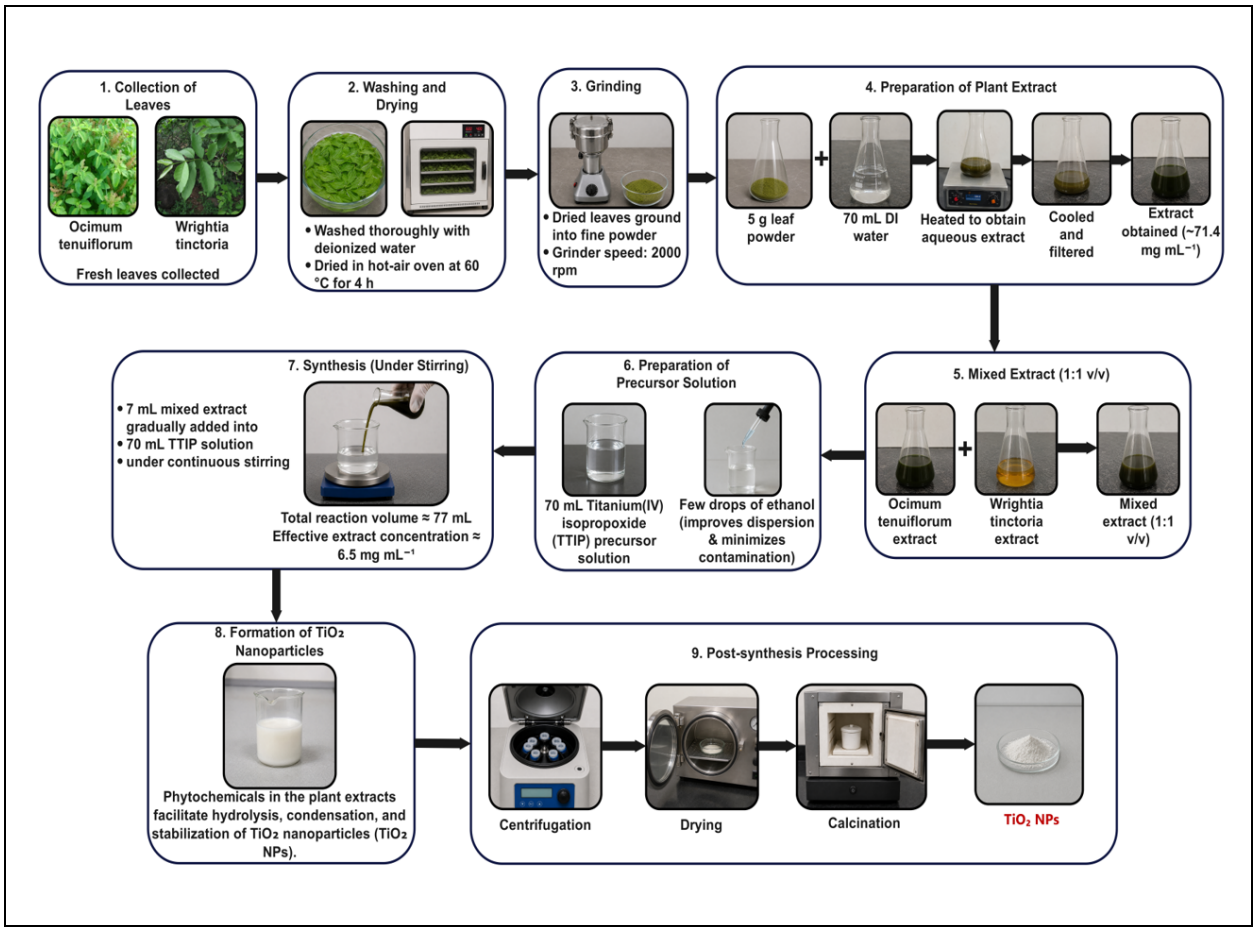


Fig. 1: Green synthesis of TiO_2 nanoparticles

2.3.5 UV–Vis Spectroscopy

Optical absorption characteristics of synthesized TiO_2 NPs were investigated by a PerkinElmer Lambda 365 UV–Visible spectrophotometer (Özcan *et al.* 2026). Absorption spectra were recorded over the wavelength range of 200–800 nm using distilled water as the reference medium. UV–Vis analysis was performed to analyse the optical response and characteristic absorption behavior of synthesized TiO_2 NPs. The optical band gap was estimated using the Tauc relationship, $(\alpha h\nu)^{1/2}=A(h\nu-E_g)$, considering the indirect allowed transition of anatase TiO_2. The band-gap energy was obtained by extrapolating the linear region of the $(\alpha h\nu)^{1/2}$ versus $h\nu$ plot to the energy axis.

2.4 Antibacterial Activity and MIC Concentration

Antibacterial activity was evaluated against *Escherichia coli* DH5α, *Enterobacter* 2282, and *Bacillus subtilis* 1305 using the agar-well diffusion method. Fresh bacterial suspensions were adjusted to a 0.5 McFarland standard, corresponding to approximately 1.5×10^8 CFU mL^{-1}. A 100 µL aliquot of each standardized suspension was uniformly spread over Mueller–Hinton agar plates. Wells with a diameter of 6 mm were prepared aseptically, and 100 µL of TiO_2 NP suspension at 25, 50, 75, 100, or 250 µg mL^{-1} was introduced into each well. Ciprofloxacin at 500 µg mL^{-1} and sterile deionized water served as the positive and negative controls, respectively. The plates were incubated at 36 ± 1 °C for 24 h, after which the inhibition-zone diameter was measured in millimetres. Each experiment was performed in triplicate (n = 3), and the results were expressed as mean ± standard deviation. Statistical differences were evaluated using one-way ANOVA followed by Tukey's post-hoc test at $p < 0.05$.

The minimum inhibitory concentration (MIC) of the synthesized TiO_2 NPs was determined using the broth microdilution method (Kim *et al.* 2024). Twofold serial dilutions of each TiO_2 NP formulation were prepared in Mueller–Hinton broth over a concentration range of 15.625–1000 µg mL^{-1}. Each well was inoculated to obtain a final bacterial density of approximately 5×10^5 CFU mL^{-1} and a final volume of 200 µL. Wells containing inoculated broth without TiO_2 NPs and uninoculated sterile broth served as the growth and sterility controls, respectively. Ciprofloxacin was included as the positive antibacterial control. The microplates were incubated at 36 ± 1 °C for 24 h. The MIC was defined as the lowest TiO_2 NP concentration that produced no visible bacterial growth relative to the growth control. All measurements were performed in triplicate (n = 3).

2.5 Machine Learning-based Prediction of TiO_2 Nanoparticle Cytotoxicity and Cell Viability

A supervised machine learning framework was developed to estimate the cytotoxic response and cell viability of green-synthesized TiO_2 NPs under different experimental conditions. The predictive model was implemented using a gradient boosting regression algorithm to establish the relationship between physicochemical characteristics of TiO_2 NPs and corresponding biological responses. A computationally constructed dataset of 240 observations was used exclusively for machine-learning model development. These observations were not generated through direct mammalian-cell experiments and were not extracted from individual published cytotoxicity datasets. The dataset was structured from three TiO_2 NP formulations, ten concentration levels (10, 25, 50, 75, 100, 150, 200, 300, 400, and 500 µg mL^{-1}), two exposure periods (24 and 48 h), and four cell lines (HeLa, HEK-293, J774A.1, and HepG2), giving $3 \times 10 \times 2 \times 4 = 240$ observations. Therefore, the resulting ML predictions should be interpreted as preliminary computational estimates requiring subsequent experimental cytocompatibility validation.

Prior to model development, the dataset was examined for missing observations and inconsistent entries. Numerical variables were normalized, while categorical information corresponding to the cell lines was transformed into a machine-readable format through one-hot encoding. Model performance was evaluated using grouped 10-fold cross-validation. Each unique combination of TiO_2 NP formulation, concentration, and exposure duration was treated as one group, and all four cell-line observations belonging to that exposure condition were assigned to the same fold. Consequently, observations representing the same physicochemical exposure condition could not occur simultaneously in the training and validation subsets. Model performance was quantified using coefficient of determination (R^2), root mean square error (RMSE), mean absolute error (MAE), and mean absolute percentage error (MAPE) (Ebenezer *et al.* 2026).

Final gradient boosting model was trained using optimized hyperparameters, including 300 learning iterations, a learning rate of 0.03, and shallow regression trees to minimize overfitting while maintaining high prediction accuracy. Following model training, predicted cell viability values were obtained for all experimental conditions. The corresponding cytotoxicity (%) was determined according to (Sajer *et al.* 2024):

$$\text{Cytotoxicity (\%)} = 100 - \text{Predicted Cell Viability (\%)} \quad \ldots (2)$$

To facilitate biological interpretation, concentration-dependent viability and cytotoxicity profiles were generated for each cell line at both exposure periods. In addition, predictor importance analyses were performed to quantify the relative influence of all experimental parameters on model output. The resulting regression performance, residual distribution, feature importance, dose-response characteristics, and heatmap visualization collectively provided a comprehensive assessment of the predictive behavior of the developed ML model for TiO_2 nanoparticle-induced cytotoxicity.

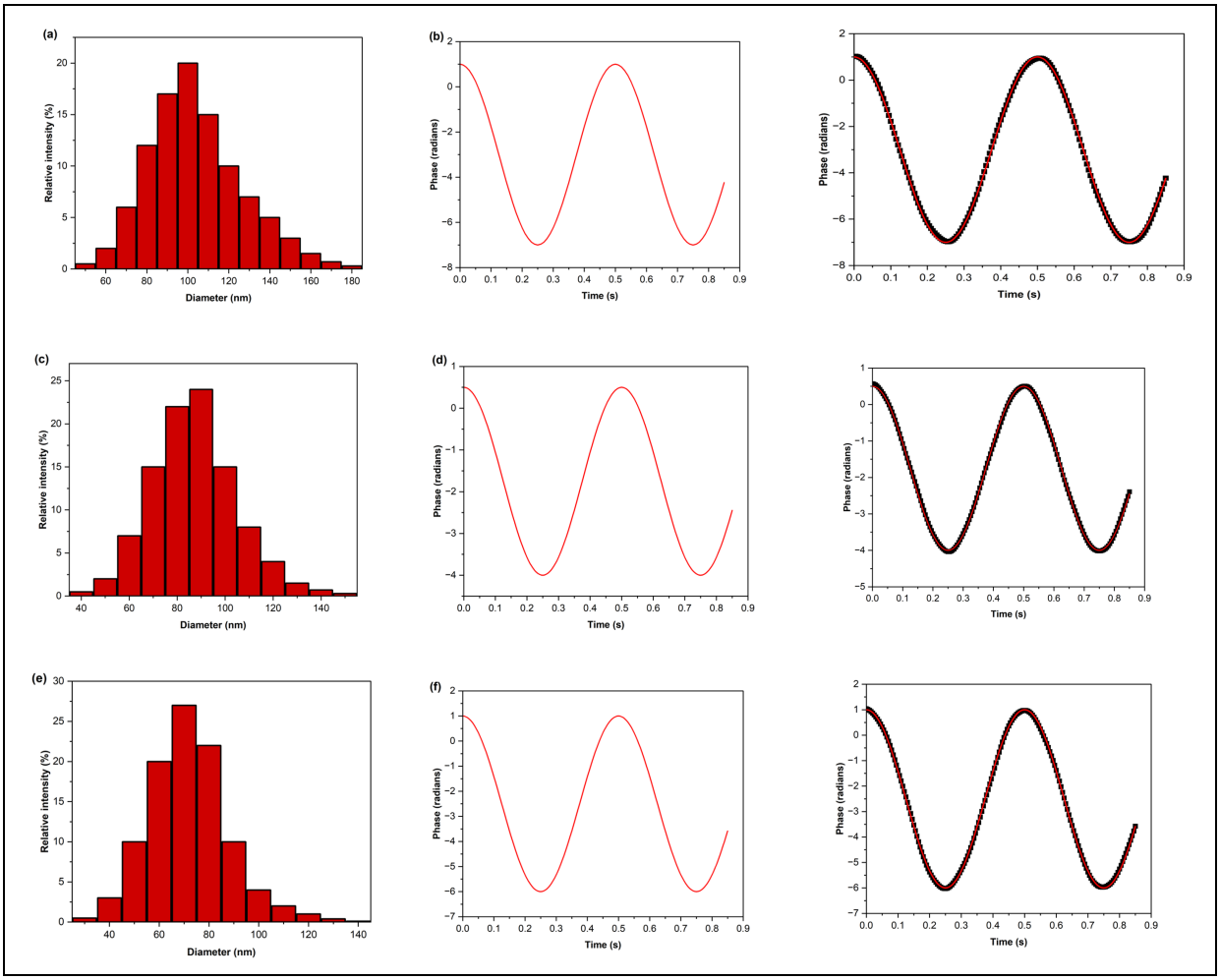


Fig. 2: DLS and zeta potential profiles (a, c, and e) hydrodynamic size distributions and (b, d, and f) zeta potential profiles of TiO_2 NPs

3. RESULTS AND DISCUSSION

3.1 DLS Analysis

Hydrodynamic particle size and colloidal stability of TiO_2 NPs were evaluated by DLS and electrophoretic light scattering. Prior to measurement, nanoparticle suspensions were dispersed in deionized water and ultrasonicated for 15 minutes to minimize particle agglomeration and ensure uniform dispersion. The average hydrodynamic diameter was calculated from the scattered light intensity generated by the Brownian motion of the nanoparticles. Zeta potential was measured using disposable folded capillary cells, and each sample was analyzed in triplicate. Measured particle size distributions, zeta potential values, and pass percentages were summarized in Table 1. Corresponding particle size distribution and zeta potential profiles are presented in Fig. 1.

The percentages of 57.7%, 85.5%, and 96.5% represent the instrument-derived cumulative fractions of the *O. tenuiflorum*, *W. tinctoria*, and combined-extract samples, respectively, occurring below a hydrodynamic diameter of 100 nm.

Table 1. Hydrodynamic diameter, cumulative fraction below 100 nm, and zeta potential of TiO_2 NP suspensions

S. No.	Sample	Pass Percentage	Average Size	Zeta Potential
1	TiO_2 NPs (*Ocimum tenuiflorum* extract)	57.7	103.6	−24.8
2	TiO_2 NPs (*Wrightia tinctoria* extract)	85.5	87.1	−27.1
3	TiO_2 NPs (Mixed leaf extracts)	96.5	71.9	−31.2

The dynamic light scattering results revealed that synthesized TiO_2 NPs possessed hydrodynamic diameters predominantly within the nanoscale region. As illustrated in Fig. 2(a), the principal particle population was centered at approximately 100 nm, with nearly 58% of the particles below 100 nm. A minor fraction of particles between 150 and 180 nm was also detected, which is attributed to limited aggregation during suspension. The particle-size profile shown in Fig. 2(c)

exhibited a similar distribution, although the dominant peak shifted slightly toward 90 nm, indicating a broader size distribution. In Fig. 2(e), the mixed-extract sample displayed the narrowest distribution, with most particles ranging from 50 to 90 nm, suggesting improved dispersion stability. The corresponding zeta potential measurements confirmed stable colloidal behavior with all samples exhibiting negative surface charges ranging from −24.8, −27.1, and −31.2 mV, indicating effective electrostatic stabilization provided by phytochemical capping molecules. These observations demonstrate that the synthesized TiO_2 nanoparticles remained well dispersed in aqueous suspension with only slight agglomeration. Similarly, green-synthesized silver nanoparticles using *Withania coagulans* leaf extract exhibited an average particle size of 26.63 nm (Khan *et al.* 2025). The DLS values of 103.6, 87.1, and 71.9 nm represent the hydrodynamic diameters of the *O. tenuiflorum*, *W. tinctoria*, and combined-extract samples, respectively, including their associated solvation layers and any dispersed aggregates. In contrast, the XRD values of 13, 15, and 18 nm represent coherent crystalline-domain sizes, whereas the FESEM ranges describe primary-particle dimensions observed in the dried state. Therefore, DLS hydrodynamic diameter, XRD crystallite size, and FESEM particle size characterize different structural features and should not be directly compared or used interchangeably.

3.2 XRD Analysis

XRD was performed to determine the phase composition and crystalline structure of synthesized TiO_2 NPs. Diffraction patterns were indexed using the ICDD/JCPDS reference database. All samples exhibited diffraction peaks characteristic of the anatase TiO_2 phase, confirming successful crystallization without detectable secondary phases. The calculated crystallite sizes and corresponding dominant diffraction planes were summarized in Table 3.

Table 2. Crystallite size comparison

S. No.	Sample	Dominant Planes	Average Crystallite Size
1	TiO_2 NPs (*Ocimum tenuiflorum* extract)	(101), (200)	13
2	TiO_2 NPs (*Wrightia tinctoria* extract)	(101), (200)	15
3	TiO_2 NPs (Mixed leaf extracts)	(101), (200)	18

X-ray diffraction patterns of synthesized TiO_2 nanoparticles are presented in Fig. 3. All three samples exhibited characteristic diffraction peaks at 2θ values of 25.30°, 37.80°, 48.05°, 53.89°, 55.06°, 62.69°, 68.76°, 70.31°, 75.03°, and 82.66°, corresponding to (101), (004), (200), (105), (211), (204), (116), (220), (215), and (224) crystallographic planes of anatase TiO_2, respectively.

The TiO_2 NPs synthesized using *Ocimum tenuiflorum* extract exhibited comparatively broader diffraction peaks and an average crystallite size of 13 nm. The *Wrightia tinctoria*–mediated TiO_2 NPs displayed moderately sharper peaks, corresponding to an average crystallite size of 15 nm. Likewise, in a previous study, green-synthesized silver nanoparticles using *Withania coagulans* leaf extract exhibited a crystallite size of 39.76 nm and an average particle size of 26.63 nm (Khan *et al.* 2025). The combined-extract TiO_2 NPs produced the sharpest and most intense reflections, indicating comparatively greater crystallinity and an average crystallite size of 18 nm. No additional peaks attributable to rutile TiO_2 or other titanium-containing impurity phases were detected, confirming formation of phase-pure anatase TiO_2.

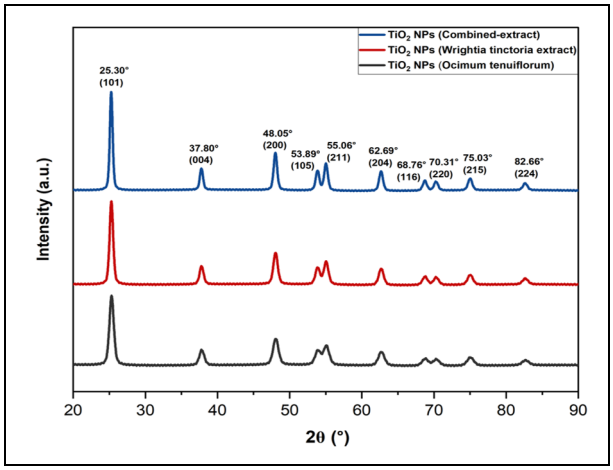


Fig. 3: XRD patterns of TiO_2 NPs

3.3 FTIR Spectroscopy Analysis

FTIR spectroscopy was employed to identify functional groups associated with synthesized TiO_2 NPs and to examine interactions between plant-derived phytochemicals and the nanoparticle surface. Spectra were recorded over the wavenumber range of 4000–500 cm^{-1} with a spectral resolution of 4 cm^{-1}. The observed absorption bands indicate the participation of naturally occurring biomolecules during the hydrolysis of Titanium(IV) isopropoxide (TTIP) and the subsequent stabilization of TiO_2 NPs.

FTIR spectrum of TiO_2 nanoparticles synthesized by *Ocimum tenuiflorum* leaf extract exhibited broad absorption at approximately 3423 cm^{-1}, attributed to O–H stretching vibrations of surface hydroxyl groups. The peak at 2927 cm^{-1} was assigned to aliphatic C–H stretching, while the absorption band at 1635 cm^{-1} was assigned to H–O–H bending and residual C=O groups. Bands at 1387 cm^{-1}, 1113 cm^{-1}, and 1045

cm^{-1} were attributed to C–H bending, C–O stretching, and C–O–C stretching vibrations, respectively. The low-wavenumber bands at 803 cm^{-1}, 628 cm^{-1}, and 524 cm^{-1} corresponded to Ti–O–Ti vibration, Ti–O–Ti stretching, and Ti–O lattice vibration, respectively.

The spectrum of TiO_2 nanoparticles prepared by Wrightia tinctoria leaf extract displayed a broad O–H band at 3418 cm^{-1}, together with characteristic C–H peaks at 2922 cm^{-1}. The absorption band at approximately 1630 cm^{-1} was assigned to H–O–H bending and residual carbonyl groups. Peaks at 1382 cm^{-1}, 1108 cm^{-1}, and 1040 cm^{-1} were attributed to C–H bending, C–O stretching, and C–O–C stretching vibrations, respectively. The characteristic bands observed at 798 cm^{-1}, 615 cm^{-1}, and 518 cm^{-1} corresponded to Ti–O–Ti vibration, Ti–O–Ti stretching, and Ti–O, respectively, confirming successful TiO_2 nanoparticles.

FTIR spectrum of TiO_2 nanoparticles from combined plant extracts exhibited spectral characteristics of both individual extracts. Broad hydroxyl absorption appeared at approximately 3416 cm^{-1}, accompanied C–H stretching bands at 2921 cm^{-1}. The absorption band at 1629 cm^{-1} was attributed to H–O–H bending and residual C=O groups. Bands observed at 1381 cm^{-1}, 1107 cm^{-1}, and 1039 cm^{-1} were assigned to C–H bending, C–O stretching, and C–O–C stretching vibrations, respectively. Low-wavenumber absorption bands at 797 cm^{-1}, 610 cm^{-1}, and 515 cm^{-1} corresponded to Ti–O–Ti vibration, Ti–O–Ti stretching, and Ti–O vibration, respectively. The coexistence of carbonyl, hydroxyl, and oxygen-containing groups shows that phytochemicals present in plant extracts participated in nanoparticle formation and remained adsorbed on the TiO_2 surface, enhancing nanoparticle stabilization and dispersion. FTIR of synthesized TiO_2 NPs was presented in Fig. 4.

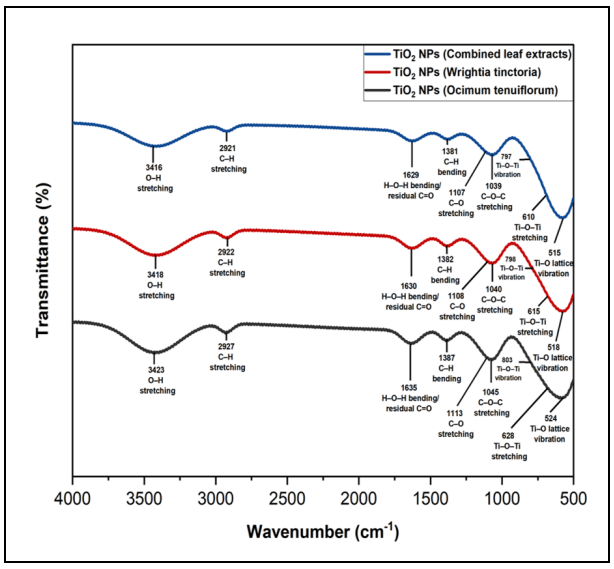


Fig. 4: FTIR spectra of TiO_2 NPs

3.4 FESEM and EDX Evaluation

FESEM micrographs acquired at various magnifications were used to analyse the average particle size of synthesized TiO_2 NPs, presented in Fig. 5(a–c). The images were recorded using a Gemini Zeiss field emission scanning electron microscope, providing information on surface texture, particle shape, and agglomeration. Elemental composition of synthesized TiO_2 NPs was subsequently analyzed by an integrated EDS detector to verify the presence and distribution of titanium and oxygen.

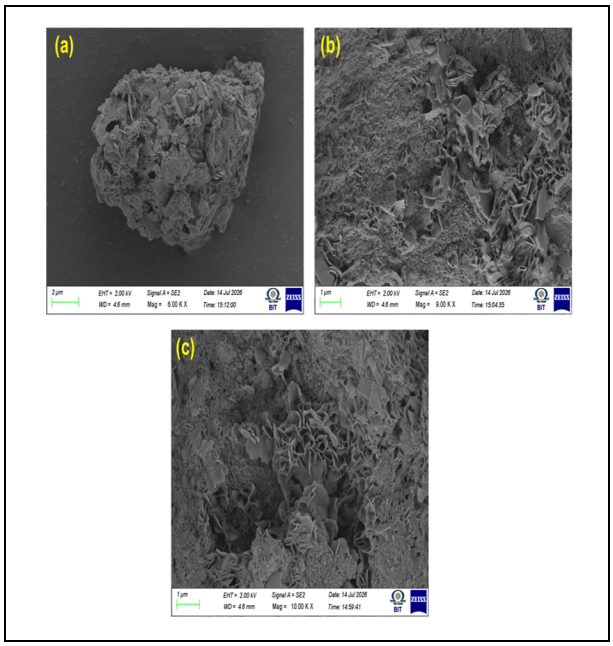


Fig. 5: FESEM images of TiO_2 NPs

The low-magnification FESEM images in Fig. 5(a–c) were used to examine the overall morphology and agglomeration of the synthesized TiO_2 NPs. The *O. tenuiflorum*-mediated sample exhibited irregular plate-like particles distributed within rough and porous agglomerates, whereas the *W. tinctoria*-mediated sample showed plate-like and flower-like structures with noticeable particle association. The combined-extract sample also formed micron-scale secondary agglomerates during drying; however, its constituent primary particles exhibited comparatively greater morphological uniformity and a narrower size distribution. Primary-particle dimensions were estimated separately from calibrated high-magnification FESEM images used to construct the histograms in Fig. 7. The approximate size ranges were 20–70 nm for the *O. tenuiflorum* sample, 20–70 nm for the *W. tinctoria* sample, and 18–38 nm for the combined-extract sample. Therefore, the improved uniformity of the combined-extract sample refers to its primary particles and does not indicate the absence of secondary agglomeration. Elemental composition was subsequently examined

using EDS to confirm the predominant inclusion of oxygen and titanium in the synthesized samples.

The corresponding EDS spectrum presented in Fig. 6(a–c) confirmed the inclusion of titanium and oxygen, with weight percentages of 38.6% and 58.2% and atomic percentages of 61.95% and 31.21%, demonstrating successful formation of high-purity TiO_2 nanoparticles (TiO_2 NPs) with a uniform elemental composition.

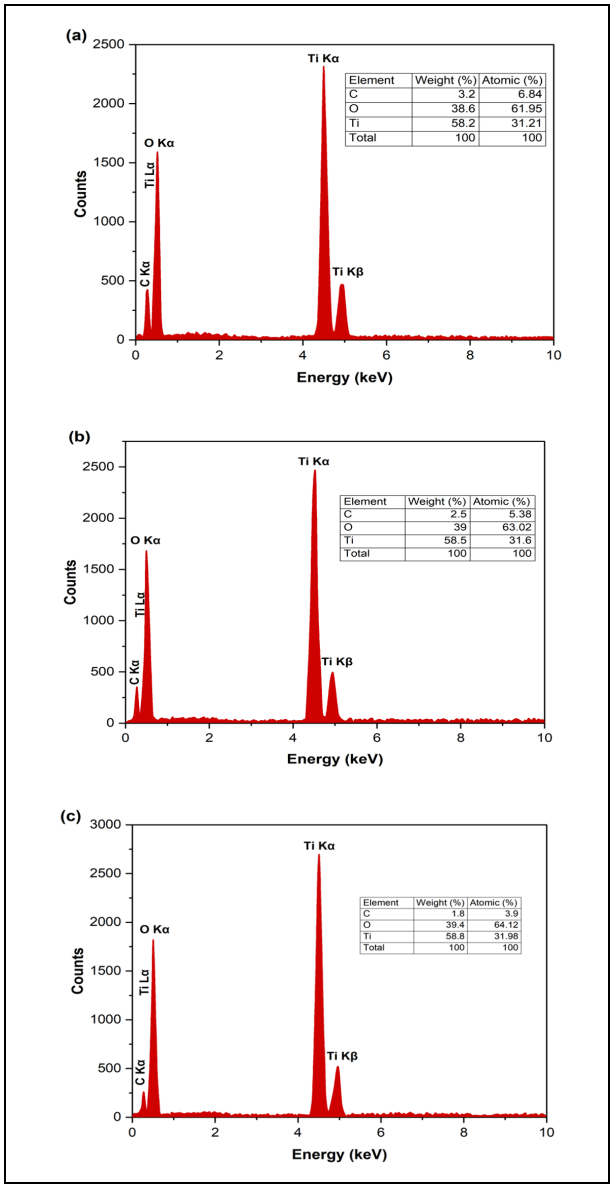


Fig. 6: EDS spectra of TiO_2 NPs

The TiO_2 nanoparticles (TiO_2 NPs) using *Wrightia tinctoria* leaf extract exhibited relatively small, well-dispersed particles with distinct boundaries and only moderate agglomeration. Based on the 300 nm scale bar, particle size ranged from approximately 30 to 80 nm. The corresponding EDS spectrum confirmed titanium and oxygen as dominant elements with weight percentages of 58.5% and 39%, and atomic percentages of 31.6% and 63.02%, showing the formation of chemically pure TiO_2. The TiO_2 nanoparticles (TiO_2 NPs) synthesized using the combined *Ocimum tenuiflorum* and *Wrightia tinctoria* leaf extracts displayed nearly spherical particles with uniform morphology, reduced agglomeration, and a narrow particle size distribution of approximately 25–70 nm. The EDS spectrum showed oxygen and titanium weight percentages of 39.4% and 58.8% and atomic percentages of 64.12% and 31.98%, respectively.

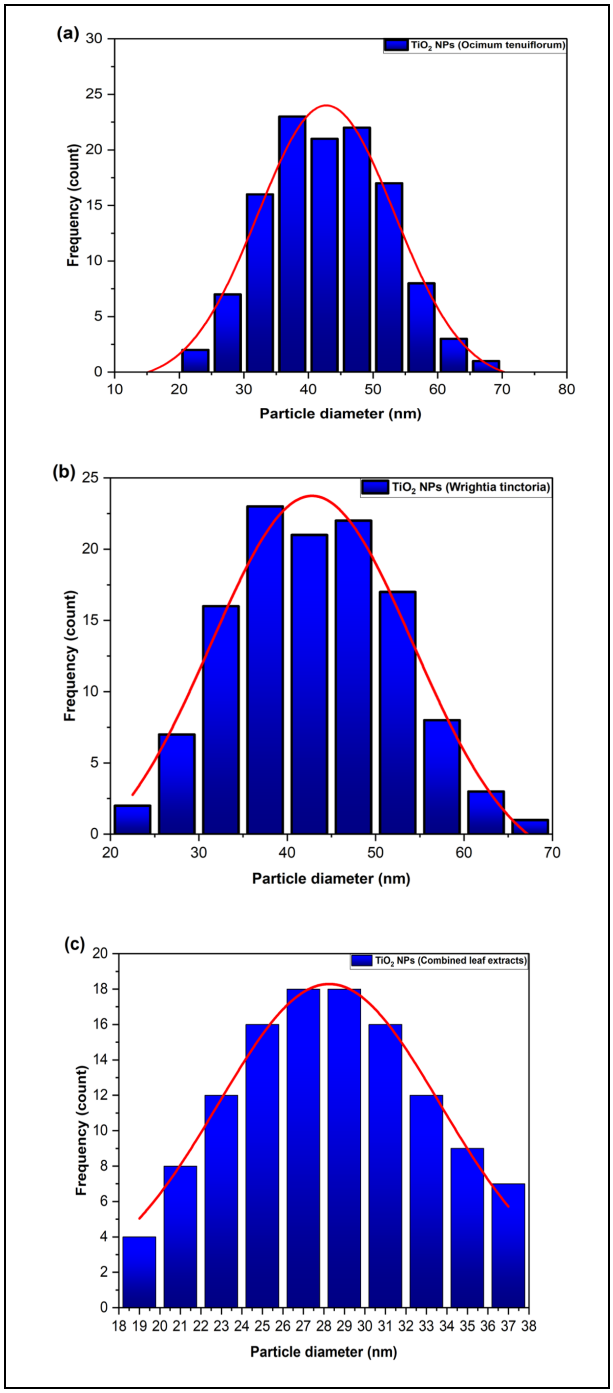


Fig. 7: Particle size distribution

The improved homogeneity suggests the cooperative stabilizing effect of phytochemicals present in both extracts. Corresponding particle size distribution were presented in Fig. 7.

The EDS spectrum of the TiO_2 nanoparticles (TiO_2 NPs) synthesized using the combined *Ocimum tenuiflorum* and *Wrightia tinctoria* leaf extracts showed titanium and oxygen weight percentages of 58.8%, 39.4%, and 1.8%, respectively, with corresponding atomic percentages of 31.98%, 64.12%, and 3.90%. Compared with individual plant extracts, the mixed-extract sample showed a more uniform elemental distribution and improved particle homogeneity. Variations in elemental composition among samples are attributed to differences in phytochemical constituents, which influence the hydrolysis of Titanium (IV) isopropoxide (TTIP) and the stabilization of the growing TiO_2 nanoparticles (TiO_2 NPs). The combined extract provided more effective control over nanoparticle morphology, resulting in reduced agglomeration and a narrower particle size distribution of approximately 18–38 nm, centred at approximately 28 nm. These observations indicate that the composition of the plant extracts plays an important role in regulating nanoparticle growth and surface characteristics.

The particle size histograms for all synthesized samples were presented in Fig. 7(a–c). The approximate particle-size ranges were 20–70 nm for the *Ocimum tenuiflorum* sample, 20–70 nm for *Wrightia tinctoria* sample, and 18–38 nm for combined-extract sample. A weak carbon peak near 0.28 keV were observed in EDS spectra and is attributed to carbon tape, residual organic compounds, or electron beam-induced surface contamination during FESEM analysis. Such carbon signals are commonly encountered in electron microscopy and do not interfere with the quantitative determination of titanium and oxygen. Proper sample handling, reduced beam exposure, and storage under clean conditions can further minimize surface contamination during elemental analysis.

3.5 UV Spectroscopy Analysis

The UV–Visible spectra of synthesized TiO_2 NPs were presented in Fig. 8. The nanoparticles synthesized using *Ocimum tenuiflorum* leaf extract (Fig. 8a) exhibited a pronounced absorption edge in the 320–340 nm region with a maximum absorbance of approximately 1.15 a.u. at 340 nm, showing the characteristic absorption behaviour of TiO_2, while nanoparticle formation and phase identity were confirmed collectively by XRD, FTIR, and EDS. Likewise, the sample prepared using *Wrightia tinctoria* leaf extract (Fig. 8b) displayed a characteristic absorption band centered near 335 nm with a slightly lower absorbance of approximately 1.29 a.u., indicating successful TiO_2 nanoparticle formation. The minor variation in absorption intensity between the two samples were attributed to variations in particle size and phytochemical composition of plant extracts, which influence nanoparticle growth and optical behavior. Tauc analysis produced approximate optical band-gap values of 3.65, 3.70, and 3.76 eV for the *O. tenuiflorum*, *W. tinctoria*, and combined-extract samples, respectively. The slight increase for the combined-extract sample is consistent with its shorter-wavelength absorption edge and smaller primary-particle distribution.

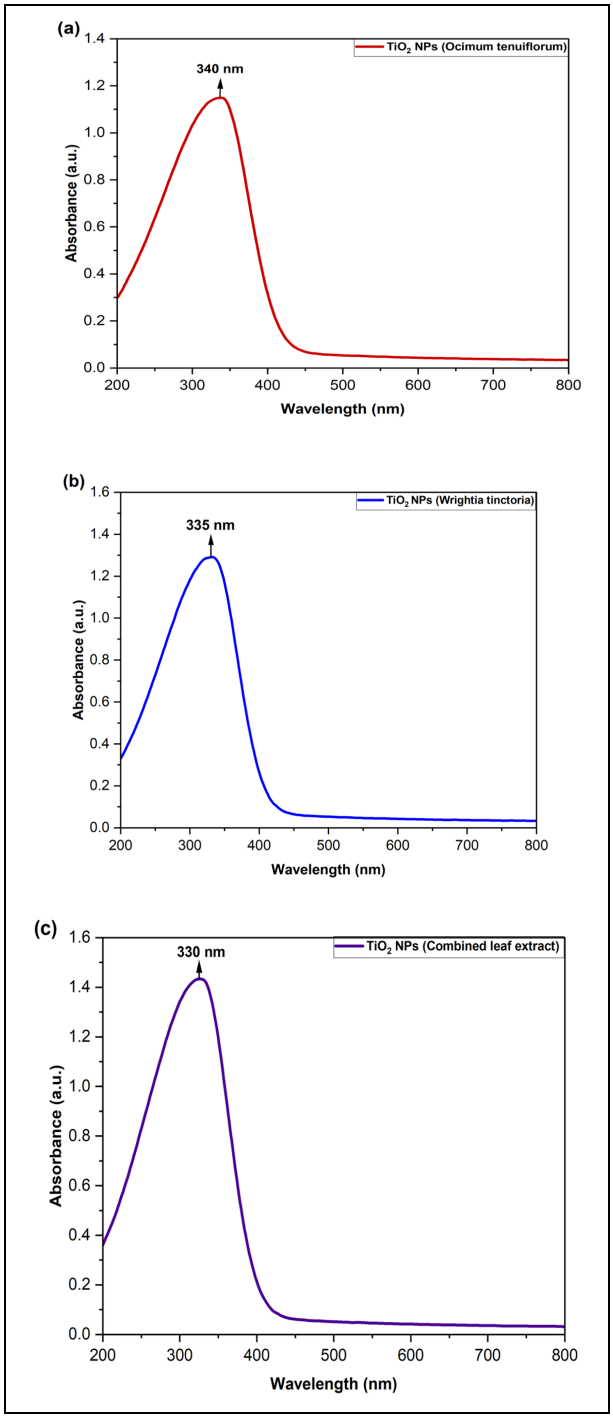


Fig. 8: UV–Visible spectra of TiO_2 NPs

Unlike metallic nanoparticles, TiO_2 does not exhibit a surface plasmon resonance band; instead, the absorption edge originates from band-gap electronic transitions of conduction and valence bands. The absorption position is influenced by crystallite size, crystallinity, and surface characteristics of synthesized nanoparticles.

The TiO_2 NPs prepared using the combined *Ocimum tenuiflorum* and *Wrightia tinctoria* leaf extracts (Fig. 8c) displayed an absorption edge near 330 nm with the highest absorbance of approximately 1.43 a.u. The shift toward a shorter wavelength suggests that phytochemicals from both extracts collectively influenced the hydrolysis and condensation of Titanium(IV) isopropoxide (TTIP), producing comparatively smaller nanoparticles. The combined-extract sample exhibited a relatively narrow particle-size distribution and reduced agglomeration. Its stronger absorption indicates effective formation and stabilization of TiO_2 NPs through the cooperative action of biomolecules from both leaf extracts.

3.6 Antibacterial Analysis

Agar medium was made according to the manufacturer's instructions and sterilized in an autoclave (Tuttnauer 3870EA, Israel) at 121 °C, 15 psi for 20 minutes. The 20 mL of sterile medium was poured into Petri dishes inside a Class II laminar airflow cabinet (Esco Airstream AC2-4S1, Singapore) and allowed to solidify under aseptic conditions (Shimi *et al.* 2022). Fresh cultures of *Enterobacter* (2282), *Bacillus subtilis* (1305) and *Escherichia coli* DH5α (GFP) were uniformly inoculated onto the agar surface. Five concentrations of TiO_2 nanoparticles (TiO_2 NPs) (25, 50, 75, 100, and 250 μg mL^{-1}) were prepared and introduced into the wells. Ciprofloxacin at 500 μg mL^{-1} served as the positive antibacterial control, while sterile deionized water served as the negative control. Inhibition zones surrounding each well were measured and recorded. Corresponding zone of inhibition (ZOI) values were summarized in Table 3.

Antibacterial performance of synthesized TiO_2 NPs varied with nanoparticle concentration and bacterial species. TiO_2 nanoparticles synthesized using *Ocimum tenuiflorum* leaf extract produced inhibition zones from 7 to 13 mm against *E. coli*, 8 to 14 mm against *Enterobacter*, and 6 to 12 mm against *Bacillus subtilis*, demonstrating progressively improved antibacterial activity with increasing concentration. The nanoparticles prepared using *Wrightia tinctoria* leaf extract exhibited moderate inhibition, reaching maximum zones of 12, 13, and 11 mm, respectively, at 250 μg mL^{-1}. TiO_2 NPs synthesized using the combined *Ocimum tenuiflorum* and *Wrightia tinctoria* leaf extracts displayed the strongest antibacterial activity, producing inhibition zones of 15 mm against *E. coli*, 16 mm against *Enterobacter*, and 14 mm against *B. subtilis*. The enhanced antibacterial efficiency of the mixed-extract sample was attributed to its smaller particle size, improved dispersion, and larger active surface area, which promote stronger interactions with bacterial cell membranes.

Table 3. Antibacterial activity of TiO_2 NPs

S. No.	Sample	Concentration	*E. coli DH5α*	*Enterobacter*	*Bacillus subtilis*
1	TiO_2 NPs (*Ocimum tenuiflorum*)	25	7	8	6
		50	9	10	8
		75	10	11	9
		100	11	12	10
		250	13	14	12
2	TiO_2 NPs (*Wrightia tinctoria*)	25	6	7	6
		50	8	9	7
		75	9	10	8
		100	10	11	9
		250	12	13	11
3	TiO_2 NPs (Mixed extracts)	25	8	9	7
		50	10	11	9
		75	12	13	11
		100	13	14	12
		250	15	16	14

Antibacterial activity increased consistently with TiO_2 NP concentration. At 250 µg mL^{-1}, the combined-extract sample produced inhibition zones of 15, 16, and 14 mm against *E. coli*, *Enterobacter*, and *B. subtilis*, respectively, compared with 13, 14, and 12 mm for the *O. tenuiflorum* sample and 12, 13, and 11 mm for the *W. tinctoria* sample. The comparatively stronger response of the combined-extract formulation may be associated with its narrower primary-particle distribution and greater accessible surface area. The concentration-dependent antibacterial response may involve increased nanoparticle–cell interactions, ROS generation, and membrane disruption; however, direct ROS and membrane-damage measurements are required to confirm this mechanism. Representative inhibition zones against the tested bacterial strains are presented in Fig. 9.

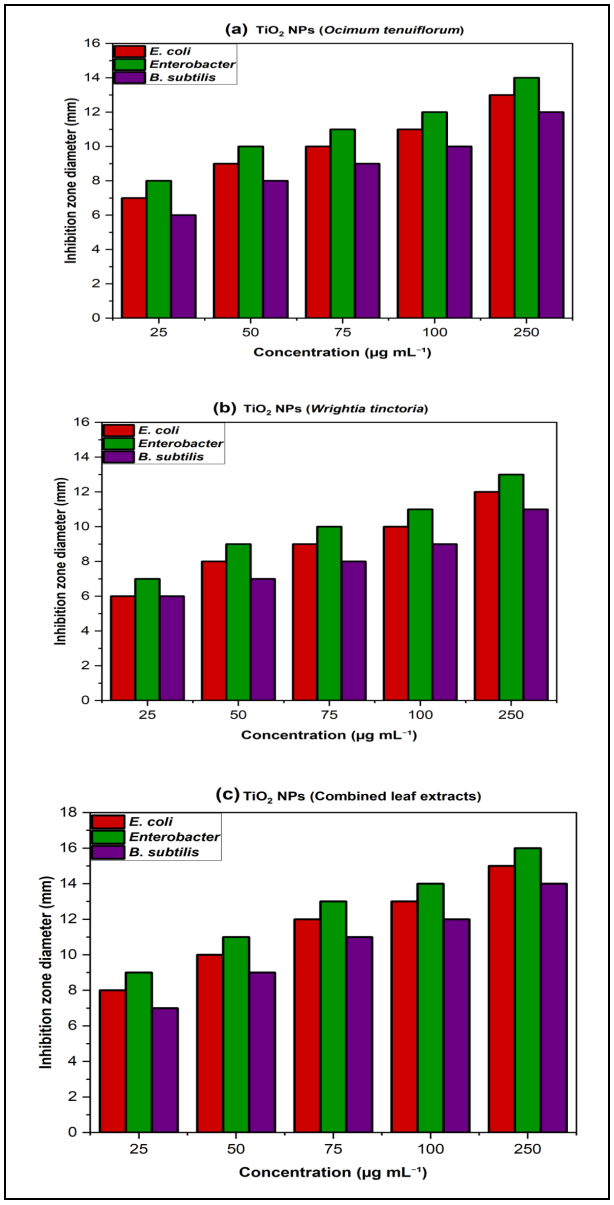


Fig. 9: Inhibition zones of TiO_2 nanoparticles against *Escherichia coli, Enterobacter, and Bacillus subtilis*

3.7 Machine Learning-based Prediction of TiO_2 Nanoparticle Cytotoxicity and Cell Viability

The developed gradient boosting regression model was employed to predict the cytotoxic response of TiO_2 NPs using six model-input variables, namely nanoparticle concentration, primary particle size, hydrodynamic diameter, zeta potential, exposure duration, and cell type. The predictive capability of the model was first evaluated through 10-fold cross-validation. As illustrated in Fig. 10a, the predicted cell viability values closely followed the corresponding experimental observations, with most data points distributed along the 1:1 reference line.

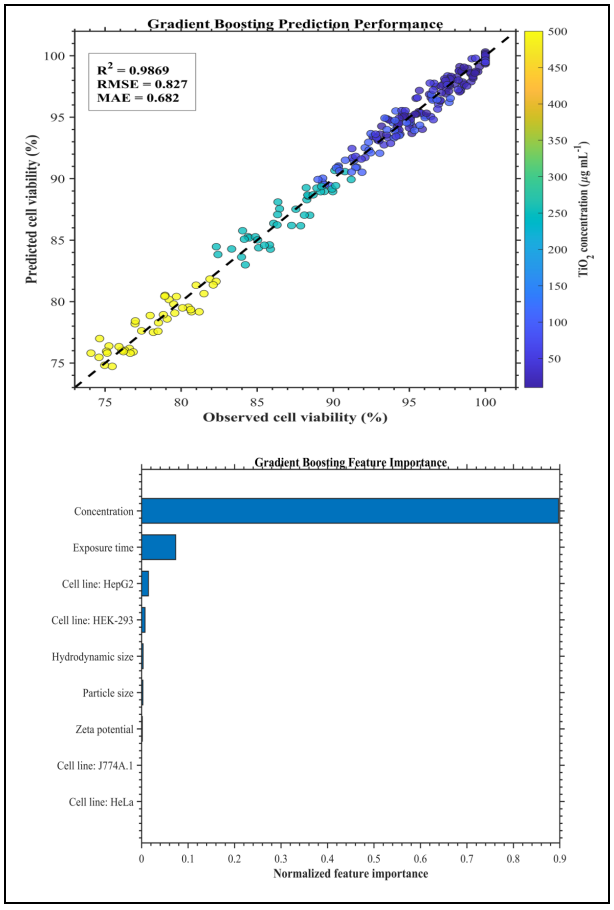


Fig. 10: Machine learning performance of the gradient boosting regression model: (A) observed versus predicted cell viability and (B) feature importance of the input variables

Under grouped 10-fold cross-validation, the model yielded R^2 = 0.9869, RMSE = 0.8267, MAE = 0.6819, and MAPE = 0.7609%, indicating strong internal performance under the adopted validation structure. These results demonstrate that the developed gradient boosting model successfully captured the nonlinear relationship among physicochemical properties of TiO_2 nanoparticles and biological responses while maintaining excellent generalization capability.

The relative contribution of each predictor variable is presented in Fig. 10b. TiO_2 NP concentration exhibited the highest feature-importance score and was therefore the most influential predictor within the developed model. Exposure duration represented the second most influential variable, whereas cell-line identity contributed moderately to the prediction. In contrast, particle size, hydrodynamic diameter, and zeta potential exhibited comparatively lower importance within the investigated experimental range. These findings indicate that concentration contributed most strongly to predictions within the investigated dataset; however, feature importance does not independently establish biological causality.

The concentration-dependent variation in predicted cell viability is illustrated in Fig. 11a and Fig. 11b for 24 and 48 h exposure periods, respectively.

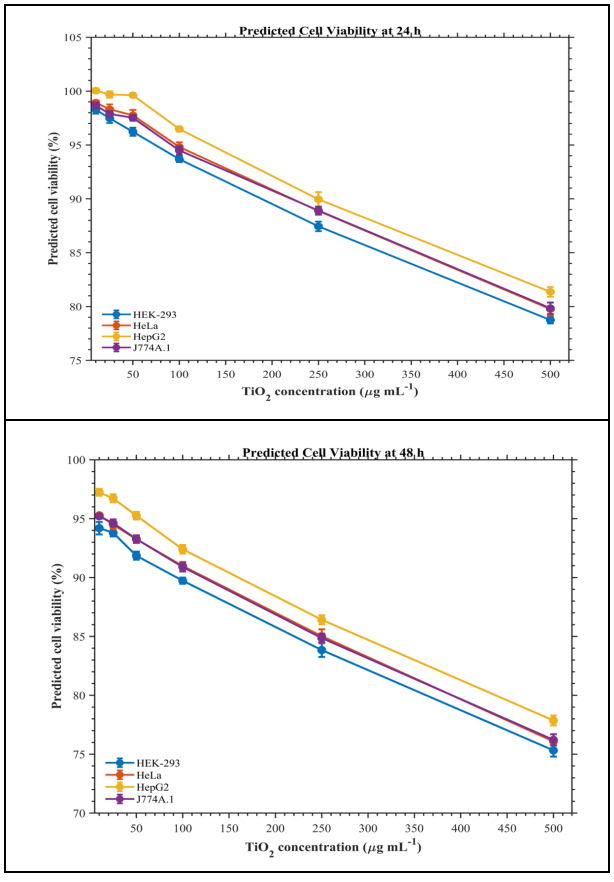


Fig. 11: Predicted cell viability of HeLa, HEK-293, HepG2, and J774A.1 cells exposed to TiO_2 nanoparticles after (A) 24 h and (B) 48 h

For all investigated cell lines, cell viability gradually decreased with increasing TiO_2 NP concentration, demonstrating a clear dose-dependent response. At lower nanoparticle concentrations (10–50 μg mL^{-1}), all cell lines maintained high viability values (>95%), indicating negligible cytotoxic effects. In a previous study, green-synthesized gold nanoparticles using Solanum marginatum leaf extract demonstrated strong anti-inflammatory potential without cytotoxicity at 6.25–12.5 μg/mL (Gebreyesus *et al.* 2026). However, progressive reductions in cell viability were observed as the concentration increased to 500 μg mL^{-1}, particularly after prolonged exposure. Comparison between the two exposure periods revealed consistently lower viability after 48 h than after 24 h, confirming the influence of exposure duration on nanoparticle-induced cytotoxicity.

Differences among the investigated cell lines were also evident. HepG2 cells retained comparatively higher viability throughout the concentration range, suggesting greater resistance to TiO_2 nanoparticle exposure. Conversely, HEK-293 cells exhibited the largest reduction in viability at elevated nanoparticle concentrations, indicating comparatively higher sensitivity. HeLa and J774A.1 cells demonstrated intermediate responses, with gradual declines in viability as nanoparticle concentration increased. These variations may be associated with differences in cellular uptake, metabolic activity, antioxidant defense mechanisms, and intracellular processing of nanoparticles among different cell types.

A comprehensive overview of the predicted biological response is presented in Fig. 12, which summarizes the mean predicted cell viability after 48 h exposure using a heatmap representation.

The gradual color transition from higher to lower viability values clearly illustrates the combined influence of nanoparticle concentration and cell type. Increasing TiO_2 NP concentration consistently reduced cell viability across all investigated cell lines, whereas HepG2 cells retained relatively higher viability compared with HEK-293, HeLa, and J774A.1 cells. The heatmap therefore provides an intuitive visualization of the concentration-dependent cytotoxic behavior predicted by the developed machine learning model and complements the individual dose-response curves.

Overall, the gradient boosting regression model accurately predicted TiO_2 nanoparticle-induced cytotoxicity and effectively identified nanoparticle concentration as the primary factor controlling cellular viability. Overall, the model provides a preliminary computational framework for prioritizing TiO_2 NP concentrations and exposure conditions for subsequent cell-based cytotoxicity experiments. The predicted viability profiles provide testable hypotheses for future MTT or equivalent assays across HeLa, HEK-293, J774A.1, and HepG2 cells.

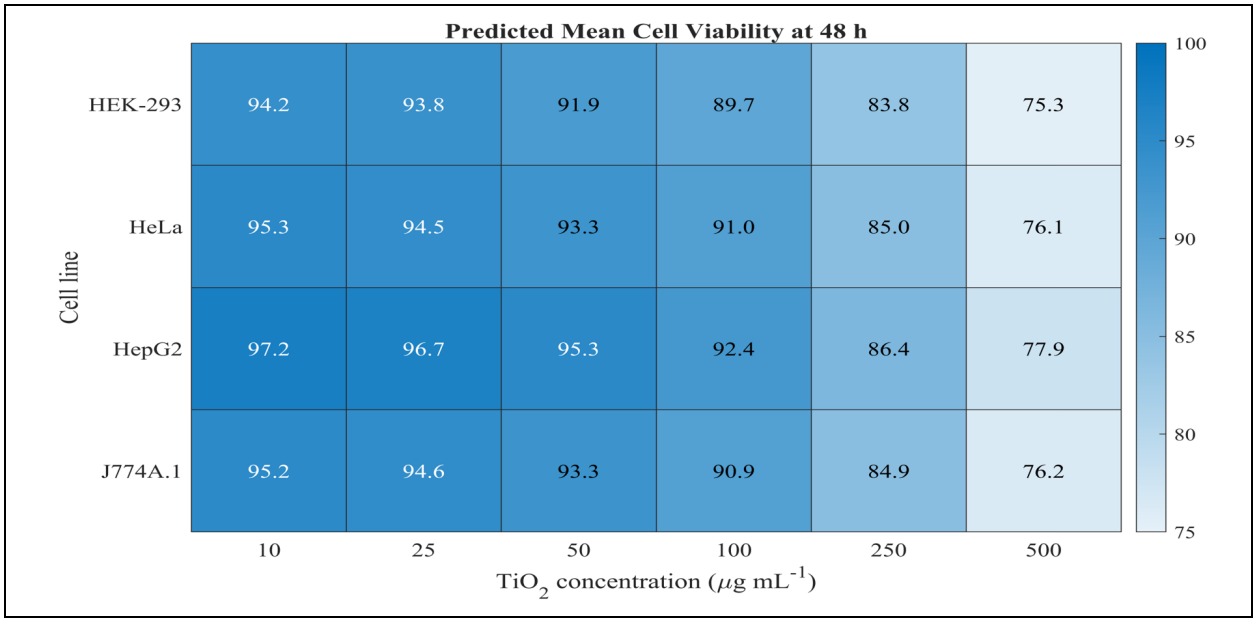


Fig. 12: Heatmap of predicted mean cell viability (%) for different TiO_2 nanoparticle concentrations after 48 h exposure

4. CONCLUSIONS

TiO_2 nanoparticles were successfully synthesized using *O. tenuiflorum*, *W. tinctoria*, and combined leaf extracts. XRD confirmed anatase TiO_2 without detectable secondary phases, with crystallite sizes of 13, 15, and 18 nm, respectively. DLS showed average hydrodynamic diameters of 103.6, 87.1, and 71.9 nm, while the corresponding instrument-derived cumulative fractions below 100 nm were 57.7%, 85.5%, and 96.5%. Zeta potentials of −24.8, −27.1, and −31.2 mV suggested progressively stronger electrostatic stabilization under the measurement conditions. FESEM revealed irregular plate-like and flower-like structures assembled into secondary agglomerates. Although micron-scale agglomeration remained evident, the combined-extract sample exhibited a comparatively narrower primary-particle range of 18–38 nm. EDS confirmed titanium and oxygen as the predominant detected elements without establishing their spatial uniformity.

All formulations demonstrated concentration-dependent antibacterial activity. At 250 µg mL^{-1}, the combined-extract sample produced inhibition zones of 16 mm against *Enterobacter* 2282, 14 mm against *B. subtilis* 1305, and 15 mm against *E. coli* DH5α. This stronger response coincided with its narrower primary-particle distribution, although BET surface-area and direct mechanistic measurements were not conducted. The gradient boosting model yielded R^2 = 0.9869, RMSE = 0.8267, MAE = 0.6819, and MAPE = 0.7609% under the adopted cross-validation procedure. Predicted viability remained above 95% at 10–50 µg mL^{-1} but decreased toward 500 µg mL^{-1}, particularly after 48 h. These computational findings support preliminary concentration screening but do not independently establish biological validity. Overall, the combined-extract route provides a sustainable approach for producing antibacterial TiO_2 NPs.

FUNDING

This research received no specific grant from any funding agency in the public, commercial, or not-for-profit sectors.

CONFLICTS OF INTEREST

The authors declare that there is no conflict of interest.

COPYRIGHT

This article is an open-access article distributed under the terms and conditions of the Creative Commons Attribution (CC BY) license (http://creativecommons.org/licenses/by/4.0/).

REFERENCES

Al-Zaqri, N., Muthuvel, A., Jothibas, M., Alsalme, A., Alharthi, F. A. and Mohana, V., Biosynthesis of zirconium oxide nanoparticles using Wrightia tinctoria leaf extract: Characterization, photocatalytic degradation and antibacterial activities, *Inorg. Chem. Commun.*, 127, 108507 (2021). https://doi.org/10.1016/j.inoche.2021.108507

Ansari, F. S. and Daneshjou, S., Optimizing the green synthesis of antibacterial TiO_2 - anatase phase nanoparticles derived from spinach leaf extract, *Sci. Rep.,* 14(1), 22440 (2024). https://doi.org/10.1038/s41598-024-73344-5

Banerjee, A., Kar, S., Pore, S. and Roy, K., Efficient predictions of cytotoxicity of TiO_2-based multi-component nanoparticles using a machine learning-based q-RASAR approach, *Nanotoxicol.*, 17(1), 78–93 (2023). https://doi.org/10.1080/17435390.2023.2186280

Blessymol, B., Kalaiselvi, V., Yasotha, P. and Gopi, S., Comparative Study of Chemically and Green Synthesized Titanium Dioxide Nanoparticles using Leucas aspera Leaf Extract, *J. Environ. Nanotechnol.,* 12(3), 10-13(2023). https://doi.org/10.13074/jent.2023.09.233471

Chandramohan, S., Nair, A. S., Das, R., Bhat, S. A., Krishna, G. S., Yadav, N., Archana, V. K. and Rajagopalan, R., Biogenic synthesis of zinc oxide nanoparticles using leaf extract of Oxalis stricta and its effect on colon cancer: an in vitro and in silico approach, *BioMetals*, 38(4), 1355–1380 (2025). https://doi.org/10.1007/s10534-025-00710-9

Chowdhury, N. R., Pritha, N., Sajid, S., Mesbah, M. B., Islam, M. E., Hakim, M., Mobarak, M. B. and Chowdhury, F., Plant-mediated green synthesis of ZnO nanoparticles utilizing Garcinia cowa leaf extract: Structural, bioactive, and in silico molecular docking insights, *Next Mater.*, 10, 101575 (2026). https://doi.org/10.1016/j.nxmate.2025.101575

Ebenezer, A. J. P., Caroline, A. L., Mayakannan, S., Dhivya, M., Sri, T. S. and Saravanan, V., Optimization of Green-synthesized Graphene Quantum Dots using Machine Learning for Neuroprotective Antioxidant Applications, *J. Environ. Nanotechnol.*, 15(2), 463–478 (2026). https://doi.org/10.13074/jent.2026.06.2622142

Ganvir, V. Y., Satishkumar, P., Awachat, D. B., Rani, A., Talodhikar, V. and Krishnaraj, C., Biofabricated CuO Nanoparticle Reinforced Bamboo Fiber Coatings for Photocatalytic Antimicrobial and Superhydrophobic Biomedical Textile Applications, *J. Environ. Nanotechnol.*, 15(2), 330–343 (2026). https://doi.org/10.13074/jent.2026.06.2622243

Gebreyesus, G. A., Welderfael, T., Chaithanya, K. K., Tekluu, B. and Berhe, T. A., Biosynthesis of gold nanoparticles from Solanum marginatum and its enhanced anti-inflammatory activity in LPS induced RAW 264.7 cell lines, *Discover Nano*, 21(1), 184 (2026). https://doi.org/10.1186/s11671-026-04634-2

Han, H. S., Jung, J. S., Jeong, Y. I. and Choi, K. C., Biological Synthesis of Copper Nanoparticles Using Edible Plant Allium monanthum: Characterization of Antibacterial, Antioxidant, and Anti-Inflammatory Properties Using In Silico Molecular Docking Analysis, *Mater.*, 16(20), 6669 (2023). https://doi.org/10.3390/ma16206669

Kadri, H. J., Rahman, M. H., Nuruzzaman, M., Ripa Khatun, M., Islam, M. M. and Mondal, M. I. H., Biocompatible and eco-friendly starch/PVA hydrogels reinforced with green-synthesised ZnO nanoparticles for advanced wound healing application, *Mater. Today Chem.*, 54, 103692 (2026). https://doi.org/10.1016/j.mtchem.2026.103692

Kamalesan, M., Raja, M., Neelamegam, R., Kamble, S. S., Shyu, D. J. H. and Nagarajan, K., Eco-Friendly Synthesis and Characterization of Calotropis gigantea-Derived Silver Nanoparticles for Combating Antibiotic-Resistant Helicobacter pylori and Gastric Cancer Cells, *Pharma.*, 19(3), 358 (2026). https://doi.org/10.3390/ph19030358

Kavikala, N., Shankar, S., Karthika, S. and Latha Maheswari, B., Phytochemical Analysis of Wrightia tinctoria Leaves and Synthesis of ZnO Nanoparticles for the Remediation of Water Pollutants, *Asian J. Chem.*, 35(4), 917–922 (2023). https://doi.org/10.14233/ajchem.2023.27575

Khan, A., Younis, T., Anas, M., Ali, M., Shinwari, Z. K., Khalil, A. T., Munawar, K. S., Mohamed, H. E. A., Hkiri, K., Maaza, M., Seleiman, M. F. and Khan, N., *Withania coagulans*-mediated green synthesis of silver nanoparticles: characterization and assessment of their phytochemical, antioxidant, toxicity, and antimicrobial activities, *BMC Plant Bio.*, 25(1), 574 (2025). https://doi.org/10.1186/s12870-025-06533-7

Kim, H. B., You, H. S., Ryu, S. J., Lee, H. Y. and Baek, J. S., Green synthesis of silver nanoparticles from mulberry leaf through hot melt extrusion: Enhanced antioxidant, antibacterial, anti-inflammatory, antidiabetic, and anticancer properties, *Food Hydrocolloids Health*, 6, 100184 (2024). https://doi.org/10.1016/j.fhfh.2024.100184

Krishnasamy, B., Gladston, A. K., Sekar, C. B. and Selvaraju, M., Investigation on the thermal, mechanical, and morphological characterization of peepal fiber-reinforced epoxy composites enhanced with micro-particulate ziziphus mauritiana seed powder, *Revista Materia*, 31, e20250643 (2026). https://doi.org/10.1590/1517-7076-RMAT-2025-0643

Najm, M. A. A., Faraj, D. N., Najim, S. S., Jabir, M. S., Jawad, K. H., Ghotekar, S., Balasubramanian, B., Ismael, A. B. and Swelum, A., CuO@MgO Nanocomposite as a Promising Strategy for Multidrug-Resistant Bacteria: A Study the Mechanism of Action via In Silico Prediction, *BioNanoSci.*, 16(6), 422 (2026). https://doi.org/10.1007/s12668-026-02665-8

Özcan, T., Çekceoğlu, İ. A., Öner, E., Ozel, S. S., Sarılmaz, A., Aslan, E., Özel, F. and Patır, İ. H., Ni- and Co-doped TiO_2 nanofibers for enhanced antibacterial and antibiofilm activities, and mechanistic insights, *Biomater. Sci.*, 14(6), 1500–1517 (2026). https://doi.org/10.1039/d5bm01721a

Ponnuswamy, M., Sathishkumar, T. P., Selvaraju, M. and Sundramurthy, V. P., Enset ventricosum Fibre-Based Biocomposite Preparation with Wood Apple Shell Particles as a Filler: Effect of Alkali Treatment and Optimization of Composition for Physio-Mechanical Properties, *Arab. J. Sci. Eng.*, 49(11), 15733–15748 (2024). https://doi.org/10.1007/s13369-024-09253-6

Rachel, D. K. S., Ramalingam, V., Venkatraman, S. M., Panneerselvam, T., Jothinathan, M. K. D., Ryntathiang, I. and Behera, A., Green Synthesis of Silver Nanoparticles from Tribulus terrestris and Investigation of Their Antioxidant and Anticancer Activities against MG-63 Osteosarcoma Cells, *Trop. J. Nat. Prod. Res.*, 9(7), 3162–3172 (2025). https://doi.org/10.26538/tjnpr/v9i7.29

Sajer, B. H., Alshehri, W. A., Alghamdi, S. S., Suliman, R. S., Albejad, A. and Hakmi, H., Aspergillus Species from the Sabkha Marsh: Potential Antimicrobial and Anticancer Agents Revealed Through Molecular and Pharmacological Analysis, *Bio. Targets Therapy*, 18, 207–228 (2024). https://doi.org/10.2147/BTT.S472491

Shehab, W. S., EL-Farargy, A. F., El-Gazzar, A. R. B. A., Haikal, H. A., Mouneir, S. M., Emwas, A. H. M., Jaremko, M. and Abdellattif, M. H., Innovation of eco-friendly TiO_2 nano catalyst for new pyrimidine carbonitiriles candidates, assessed for significant antioxidant activity, anti-inflammatory effects, and by in silico studies, *PLOS ONE*, 20(5), e0313959 (2025). https://doi.org/10.1371/journal.pone.0313959

Shimi, A. K., Ahmed, H. M., Wahab, M., Katheria, S., Wabaidur, S. M., Eldesoky, G. E., Islam, M. A. and Rane, K. P., Synthesis and applications of green synthesized TiO_2 nanoparticles for photocatalytic dye degradation and antibacterial activity, *J. Nanomater.*, 2022, 7060388 (2022). https://doi.org/10.1155/2022/7060388

Shivappa, P., Mirjankar, M. R., Gaddigal, A. T., Ganeshkar, M. P., Poojari, P. B., Huyilagola, P. V, Irannanavar, K. M., Goder, P. H. and Mukappa Kamanavalli, C., Bismuth nanoparticle synthesis utilizing hydroalcoholic Endocomia macrocoma leaf extract to evaluate their antimicrobial, antioxidant, and anticancer properties, *J. Dispers. Sci. Technol.*, 47(10), 2033-2047 (2025). https://doi.org/10.1080/01932691.2025.2462693

Silva-Jara, J. M., Juárez-Saldívar, A., Velázquez-Carriles, C. A., Anaya-Esparza, L. M., Rodríguez-Laffitte, E., Delgado-Caramutti, J., Aguilar-Uscanga, B. R., Graciano-Machuca, O., Parra-Saavedra, K. J. and Balderas-León, I., Valorization of yellow, black, and white sapote peel byproducts: exploring their antioxidant, antimicrobial, and antibiofilm properties, along with computational mapping, *J. Chem. Technol. Biotechnol.*, 101(2), 433–448 (2026). https://doi.org/10.1002/jctb.70104

Silambarasan, T., Arularasu, M. V., Vimal, S., Dhandapani, R., Selvakumar, C. and Lavanya, R., Biosynthesis and pharmaceutical properties of TiO_2-ZnO nanocomposite: Exploring density functional theory (DFT), In Silico and in vitro studies, *J. Mol. Struct.*, 1364, 145823 (2026). https://doi.org/10.1016/j.molstruc.2026.145823